arXiv:2606.04544v1 [cond-mat.mes-hall] 3 Jun 2026

Probing PbTe-Pb nanowire devices with radio-frequency reflectometry

Xin-Yi Tang,[1,2,*] Lin Li,[1,*] Zezhou Xia,[2,*] Jierong Huo,[3] Wenyu Song,[2] Lining Yang,[2] Zonglin Li,[2] Jiaye Xu,[2] Peilin Li,[2] Runan Shang,[1,4,†] Qi-Kun Xue,[1,2,3,4,5,6] Ke He,[1,2,4,6,‡] and Hao Zhang[3,5,§]

[1] *Beijing Academy of Quantum Information Sciences, Beijing 100193, China*
[2] *State Key Laboratory of Low Dimensional Quantum Physics, Department of Physics, Tsinghua University, Beijing 100084, China*
[3] *College of Semiconductors, Southern University of Science and Technology, Shenzhen 518055, China*
[4] *Hefei National Laboratory, Hefei 230088, China*
[5] *Quantum Science Center of Guangdong-Hong Kong-Macao Greater Bay Area, Shenzhen 518045, China*
[6] *Frontier Science Center for Quantum Information, Beijing 100084, China*

We report the implementation of radio-frequency (rf) reflectometry on selective-area-grown PbTe-Pb nanowire devices on a CdTe substrate. These nanowires were predicted to host Majorana zero modes. We demonstrate the compatibility of the rf technique, both resistive and capacitive sensing, with these nanowires. The effect of dielectric loss from the CdTe substrate is also discussed. The feasibility of rf reflectometry is also verified at finite magnetic fields where zero-energy modes occur. Our results enable the fast control of PbTe quantum devices, paving the way for its application in topological quantum computation.

I. INTRODUCTION

Selective-area-grown (SAG) PbTe nanowires have recently attracted much interest due to their potential application in Majorana zero modes and topological quantum computation [1–6]. After years of optimizations on material growth and device fabrication [7–18], PbTe and PbTe-Pb nanowires can now exhibit superior transport properties relative to InAs and InSb nanowires. For example, high-quality ballistic transport in long-channel PbTe nanowires and quantized Andreev plateaus in PbTe-Pb nanowires can be achieved, indicating an unprecedented low-disorder level [19–21]. Robust zero-energy modes that are consistent with Majoranas have also been reported [22, 23]. These signatures are, however, still insufficient evidence. The conclusive confirmation would be the realization of topological qubits and the demonstration of braiding operations. A key requirement of braiding is fast readout of the qubit state [24, 25]. Radio-frequency (rf) reflectometry can fulfill this demand. This technique has been implemented on III-V semiconductor devices [26–32].

Here we report the feasibility of rf reflectometry on SAG PbTe devices. Compared to the traditional InAs and InSb devices, the uncertainty comes from the device substrate CdTe and the large dielectric constant of PbTe (~ 1350). We overcome and quantify these uncertainties, and demonstrate the rf readout of PbTe-Pb and PbTe nanowire devices. We also show its compatibility with magnetic field, whose range covers the region where the zero-energy modes can emerge in this material system. Our results open the door to rf control of PbTe quantum devices, a step forward towards PbTe-based topological quantum computation.

II. EXPERIMENTAL SETUP

Figure 1(a) shows the fridge wiring of the rf reflectometry. The rf signal was generated and sent from a vector network analyzer (VNA) or an rf lock-in (upper left). After passing a high-pass filter (HPF) with a cut-off frequency of 145 MHz, the signal was fed into the dilution refrigerator via a co-axial cable. At each temperature stage within the fridge, the signal was attenuated for thermal anchoring. At the mixing chamber stage, the rf signal was fed into the device PCB through a directional coupler and a low-pass filter (LPF) with a cut-off frequency of 2 GHz. There is a 15 dB attenuation of the coupler. The total attenuation is thus ~ 54 dB, which can effectively filter out the hot photons generated at room temperature.

The photo of the device printed circuit board (PCB) is shown in Fig. 1(c). Its equivalent circuit diagram is drawn in Fig. 1(b). For a complete and more detailed view, we refer to Fig. 6 in the Appendix. The rf signal goes into a Miniature SubMiniature Push-On (Mini SMP) connector on the PCB, marked by the left orange arrow in Fig. 1(c). The center pin of the Mini SMP connector is further connected to a large capacitor ($C_{\text{interdigitated}} = 2.8$ pF) through wire bonding. Meanwhile, a dc voltage signal is added to the rf signal after passing through a 5 kΩ resistor (R_{onPCB}, lower arrow in Fig. 1(c)) and a 30 nH spiral inductor (L_{biasT}). $C_{\text{interdigitated}}$ and L_{biasT} together constitute a bias-tee that prevents the interference between the rf and dc channel. The interdigitated capacitor and spiral inductor are both fabricated on a sapphire substrate through etching of a 100-nm thick Nb film (see Appendix for details). The sapphire substrate is mounted/glued in the center void of the PCB, located next to the device chip.

* equal contribution
† shangrn@baqis.ac.cn
‡ kehe@tsinghua.edu.cn
§ zhanghao@sustech.edu.cn

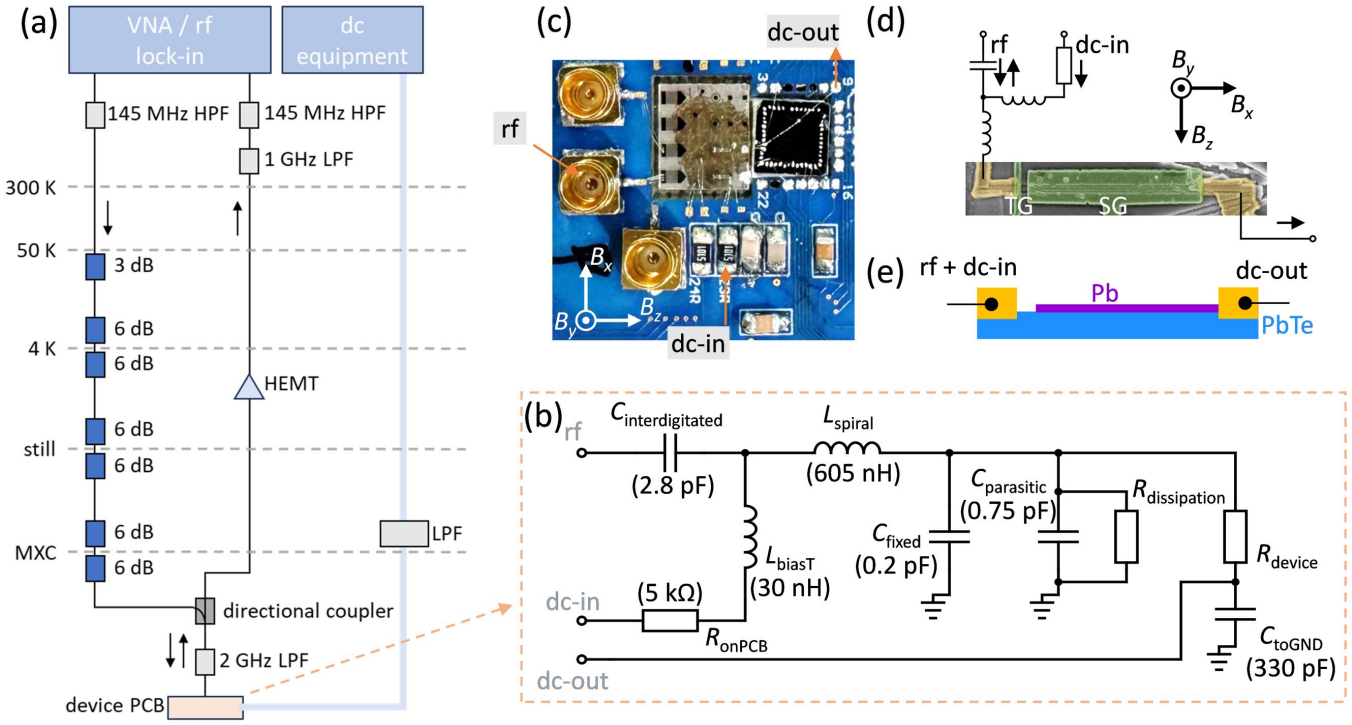

FIG. 1. rf-readout system for PbTe nanowires. (a) Schematic of fridge wiring. (b) Circuit diagram of the device PCB. The rf signal is injected from the 'rf' port. An off-chip bias-tee design enables simultaneous transport measurement through 'dc-in' and 'dc-out' ports. (c) An optical image of the device PCB, including the device chip (upper right) and a sapphire substrate carrying superconducting spiral inductors and bias-tees (the middle void). (d) False-colored SEM of the PbTe-Pb NS device. TG and SG refer to tunnel gate and super gate, respectively. (e) Simplified schematic of the device and circuit. For clarity, CdTe substrate/capping layer, PbEuTe buffer/spacing layer, gate oxide/electrodes are not drawn.

The rf and dc signals pass through an inductor (L_{spiral}), and connect to the source contact of the PbTe-Pb device through wire bonding. A ceramic capacitor on the PCB ($C_{\text{fixed}} = 0.2$ pF) is connected in parallel with the device. The device drain connects to another ceramic capacitor ($C_{\text{toGND}} = 330$ pF) and dc-out for current measurement using a pre-amplifier.

The scanning electron micrograph (SEM) of the device and a simplified circuit diagram are shown in Figs. 1(d-e). A dc bias voltage (V) is applied to the device source and the current I is measured from the drain. Meanwhile, the rf signal is sent to the LCR circuit through the rf port in Fig. 1(b). Its reflected signal is directed to another co-axial line through the directional coupler. This signal is then amplified by roughly 30 dB using a high electron mobility transistor (HEMT) at 4 K and measured at room temperature at the VNA or rf lock-in. From the perspective of PCB, the reflected signal S_{11} is measured. From the fridge circuiting, it is the transmitted signal S_{21} between two co-axial ports. In the following, we refer it as S_{21}.

The PbTe-Pb device has two top gates (TG and SG). Details of its growth and fabrication can be found in the Appendix and in our previous works [20, 22]. V_{TG} tunes the tunnel barrier while V_{SG} tunes the proximitized region as well as the barrier region due to cross talk. In the circuit diagram in Fig. 1(b), the device is represented as a gate-tunable resistor (R_{device}). In parallel, we also add a parasitic capacitor $C_{\text{parasitic}}$ and a fixed resistor $R_{\text{dissipation}}$. The former originates from the PCB, bonding pads, sample wiring, and the device. The latter is to account for the dielectric loss of the device chip. $C_{\text{parasitic}} = 0.75$ pF is extracted based on independent characterization. The value of $R_{\text{dissipation}}$ can be inferred from our simulation and will be discussed later. Note that $R_{\text{dissipation}}$ is only for the rf frequency range to account for dielectric loss. It approaches ∞ for the dc measurement.

We assume the impedance of the circuit of Fig. 1(b) at the rf port (Mini SMP) as $Z_l(\omega)$, where $\omega = 2\pi f$ is the angular frequency of the signal. The impedance of the co-axial cable is $Z_0 = 50\ \Omega$. Then from the telegraph equation [32], the reflected coefficient Γ (the ratio between the reflected signal voltage and the incident signal voltage) can be expressed as

$$\Gamma(\omega) = \frac{Z_l(\omega) - Z_0}{Z_l(\omega) + Z_0}. \tag{1}$$

In experiment, $|S_{21}|(\omega) = 20\log_{10}|\Gamma(\omega)|$ (dB) is measured. To analyze the circuit behavior near its resonance

frequency (ω_0), we do a very rough approximation by neglecting the region of the bias-tee ($C_{\text{interdigitated}}$ and L_{biasT}), as ω_0 is far away from the resonance of the bias T. C_{toGND} can also be neglected as it is shorted by the dc-out line. We can then derive

$$Z_l(\omega) \approx \mathrm{i}\omega L + (\mathrm{i}\omega C + \frac{1}{R})^{-1}, \tag{2}$$

where $L = L_{\text{spiral}}$, $C = C_{\text{fixed}} + C_{\text{parasitic}}$, $R = R_{\text{dissipation}}||R_{\text{device}} = (R_{\text{dissipation}}R_{\text{device}})/(R_{\text{dissipation}} + R_{\text{device}})$. Near the cavity resonance $\omega_0 = 1/\sqrt{LC}$, Eq. [2] can be expanded using $\omega = \omega_0 + \delta\omega$. Omitting the small terms, one can get $Z_l(\omega) \approx L/(RC)$, given that $L/(CR^2) \ll 1$. Therefore, near the circuit resonance, the gate-tunable R_{device} affects R, Z_l, and Γ, sequentially. This change of device resistance is finally readout as the change of the reflected signal power $|S_{21}|$. We note that the analysis above is based on rough approximations. For more accurate analysis, we refer to simulations (will be discussed later) including all the elements in Fig. 1(b).

III. RF AND DC PROBING OF A PbTe -Pb DEVICE

Figure 2(a) shows the rf response of the NS device measured using a VNA. The magnetic field is 0 T. The bias voltage V was set at -2 mV, i.e. outside the superconducting gap. V_{TG} was kept fixed at -5 V throughout the measurement and V_{SG} was scanned to tune the barrier region via cross talk. At $V_{\text{SG}} = -4$ V, the device is pinched off and we measured a dip in the frequency f scan, see the black curve in Fig. 2(b) for its line cut. This dip corresponds to the resonance of the LCR circuit with a resonance frequency of 241.1 MHz. As V_{SG} becomes more positive, the dip becomes smaller and finally disappears. Figure 2(b) shows this evolution with several line cuts.

This rf evolution is due to the gate-tunable device resistance/conductance in the LCR circuit. To map out the correspondence between the device conductance $G \equiv \mathrm{d}I/\mathrm{d}V$ and the reflected rf signal voltage (V_{rf}), we fixed f at 241.1 MHz, and measured both G and V_{rf} simultaneously. V_{rf} was measured using rf lock-in, while G was measured using standard two-terminal setup. R_{onPCB} and fridge filters have been subtracted and excluded from G. Figure 2(c) shows their evolution as a function of V_{SG}. Based on this correspondence, we labeled the conductance values for the line cuts in Fig. 2(b). Figure 2(d) plots V_{rf} vs G. The red curve is a polynomial fitting (between $\ln G$ and V_{rf}). Details of the fitting can be found in the Appendix.

The maximum depth of the cavity dip (the black curve in Fig. 2(b)) is ~ 3 dB. While this value is sufficient to meet our current requirement, it is small compared to the resonance signal (~ 20 dB) in rf circuits based on InAs nanowires [29]. We attributed the small dip to impedance mismatch caused by $C_{\text{parasitic}}$ and $R_{\text{dissipation}}$.

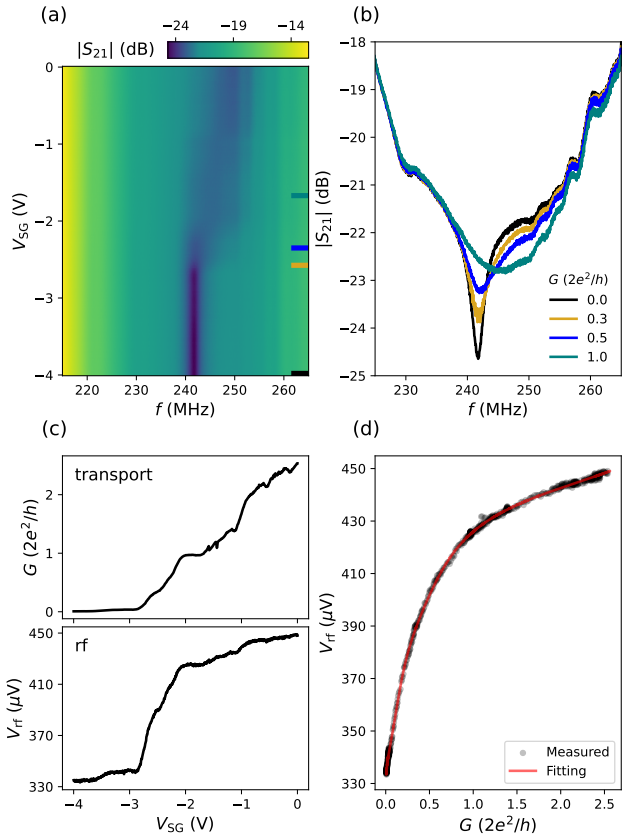

FIG. 2. Gate-tunable reflectometry. (a) $|S_{21}|$ as a function of V_{SG} and the rf frequency f. (b) Line cuts at several gate voltages (marked in (a)). (c) Transport measurement (upper) and the rf signal (lower). f is fixed at 241.1 MHz. (d) V_{rf} vs G. The red curve is the fitting.

Unlike other circuit elements whose parameters were predefined, these two terms were unknown prior to the measurement. $R_{\text{dissipation}}$ can originate from parasitic losses of the CdTe substrate, the dielectric mask (Si_3N_4), and Ag paste (used during sample wiring). To estimate their values, we performed simulation for the circuit in Fig. 1(b) using the software Advanced Design System. Based on the simulation (shown in Appendix Fig. 7), we find that $R_{\text{dissipation}}$ of 4 kΩ agrees qualitatively well with our results in terms of the dip variation for G between 0 and $2e^2/h$. L_{spiral} of 605 nH also differs from our designed value of 389 nH. This is because that the inductance of the bonding wire that connects the spiral inductor and the device is also included in L_{spiral}. This contribution can be sample and wiring dependent. The simulated circuit impedance at the resonance frequency is $Z_l = 125.2 - 5.9\mathrm{i}$ (Ω) assuming the device being pinched off. This impedance is indeed far away from 50 Ω (the impedance of the coax cable). The rough estimation using $L/(RC)$ gives 336 Ω, close to the simulation but with a sizable deviation (likely due to the omission of $C_{\text{interdigitated}}$). As the device is turned on, R decreases and Z_l increases further away from 50 Ω, resulting in a

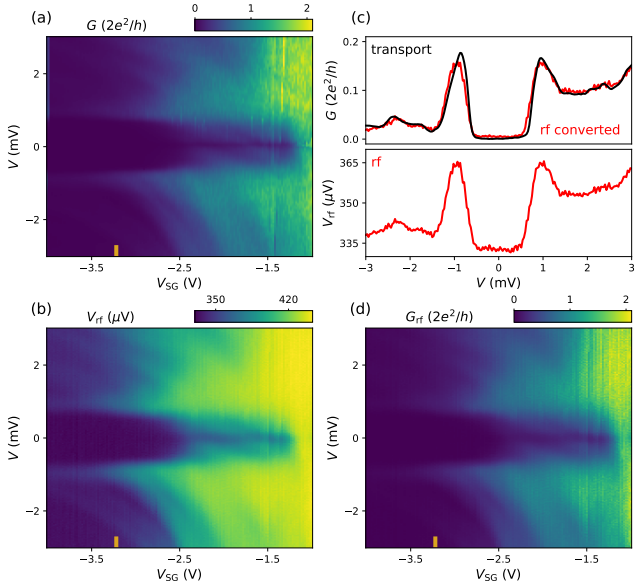

FIG. 3. Comparison of rf and dc probing of the PbTe-Pb nanowire. (a) dc conductance map as a function of V and V_{SG}. (b) rf measurement under the same gate and bias setting. (c) Line cuts from (a) (upper, black) and (b) (lower) at $V_{SG} = -3.22$ V (marked as orange bars). The red curve in the upper panel is the rf signal converted into G. (d) Conductance (G_{rf}) map converted from the rf signal in (b).

smaller dip shown in Fig. 2(b). In Fig. 5, we show circuits with better matched impedance, resulting in deeper resonance dips.

We next compare this rf method with the dc transport measurement at zero field. Figure 3(a) shows the standard conductance map of the device: G vs V and V_{SG}. A clear superconducting gap can be resolved near $\pm$ 0.9 mV. This 2D map has 201 points in bias V and 151 points in V_{SG}. The data-acquisition time is around 400 min. The frequency and time constant used in the low-frequency lock-in amplifier were set to be 33.7 Hz and 300 ms, respectively. As a comparison, a similar 2D map obtained using the rf method (Fig. 3(b)) only requires 39 min, an order of magnitude faster than the traditional dc measurement. The ranges and number of data points in gate and bias of Fig. 3(b) are identical to those in Fig. 3(a). The rf frequency was fixed at 241.1 MHz. Bandwidth and averaging times were chosen to be 8.872 kHz and 1000 respectively. Instead of the point-by-point data acquisition in the dc measurement scheme, the rf scan sends a triangular-wave-like bias signal into the device and receives the reflected signal altogether before stepping V_{SG} to the next value.

For comparison, the upper and lower panels of Fig. 3(c) are line cuts from Fig. 3(a) and Fig. 3(b) at $V_{SG} = -3.2$ V. Based on the mapping established in Fig. 2(d) (the red curve), we convert the rf signal (V_{rf}) into conductance (G_{rf}) and plot it as the red curve in the upper panel of Fig. 3(c). The transport and rf measurement agree reasonably well. For completeness, Fig. 3(d) shows the full conductance map (G_{rf}) converted from Fig. 3(b). The color bar in Fig. 3(d) is identical to that in Fig. 3(a). We note that V is the bias drop on the device, fridge filters, and R_{onPCB}. The order-of-magnitude reduction in data-acquisition time offers a significant advantage by accelerating the exploration of PbTe-Pb devices for Majorana searching.

IV. MAGNETIC FIELD COMPATIBILITY

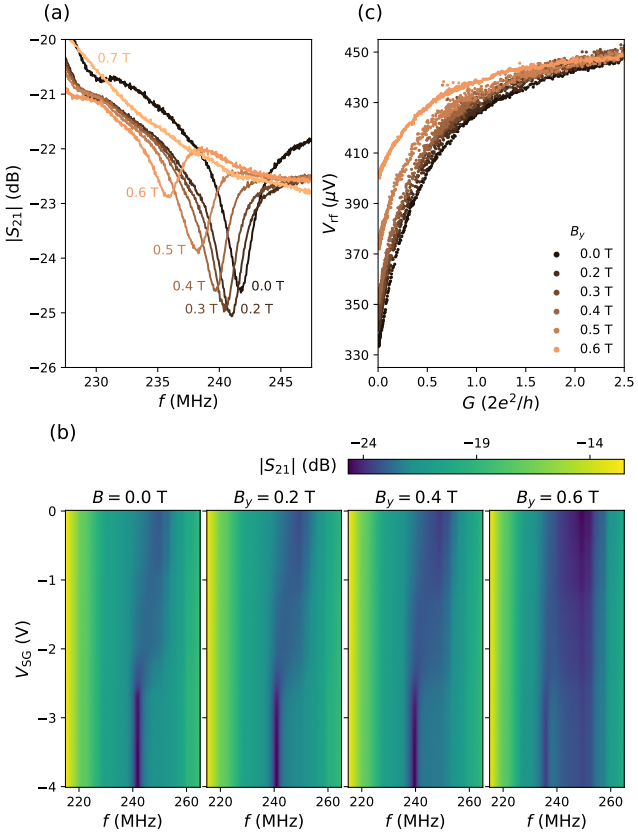

FIG. 4. Magnetic field compatibility. (a) The resonator response at different B_y's (out-of-plane). V_{SG} is fixed at -4.0 V. (b) The reflectometry signal as a function V_{SG} at B_y of 0.0, 0.2, 0.4, 0.6 T, respectively. (c) rf signal (V_{rf}) vs G obtained at different fields.

We next verify the feasibility of this technique with magnetic field (B), especially for the field range where Majorana zero modes may occur. We have reported possible Majorana signatures in PbTe-Pb nanowires [22, 23]. The optimal B is near 0.2 T and its direction is nearly out-of-plane, i.e. B_y (see Figs. 1(c-d) for the coordinate axes). Figure 4(a) shows the resonator response by applying B along this direction. The NS device is pinched off, i.e. $V_{SG} = -4$ V. As B_y increases, the resonance shifts towards lower frequency. We attribute this shift to the increase of kinetic inductance of the superconducting spiral inductors, as the magnetic field reduces the Cooper

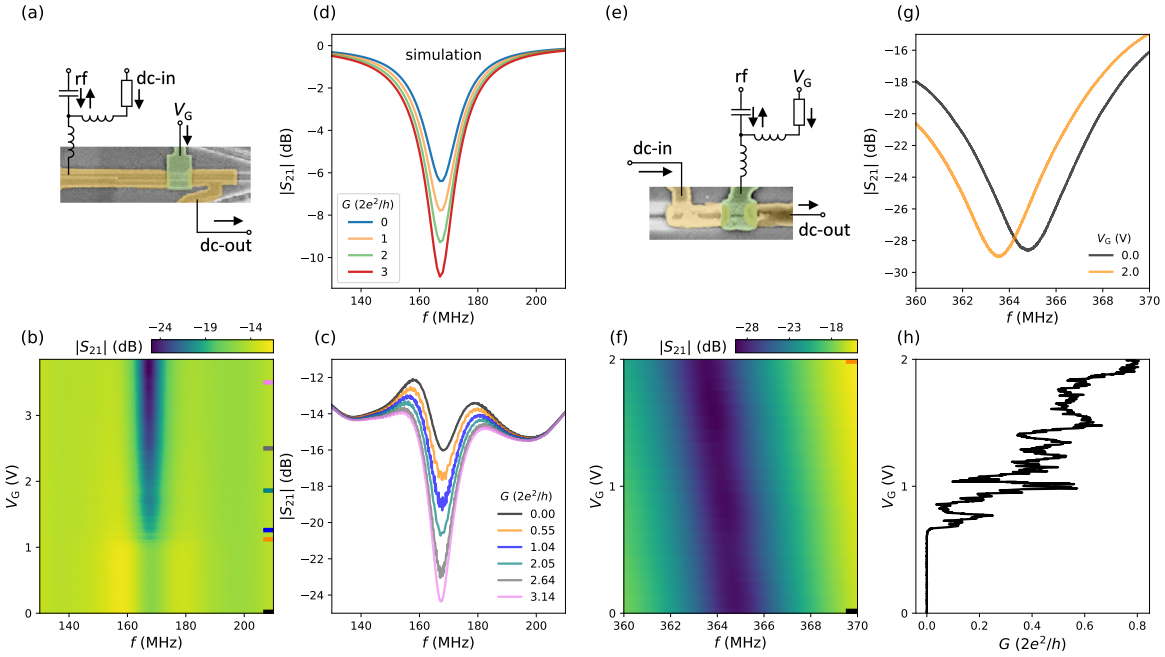

FIG. 5. Resistive and capacitive sensing of PbTe field effect devices. (a) SEM of a PbTe device using the resistive readout. (b) $|S_{21}|$ as a function of V_G and the rf frequency. (c) Line cuts at several gate voltages marked in (b). (d) Simulated cavity response for different device conductance. (e) SEM of a PbTe device using capacitive readout. (f) $|S_{21}|$ as a function of V_G and the rf frequency. (g) Two line cuts from (f) at $V_G = 0$ V and 2 V, respectively. (h) Conductance of this device as a function of V_G. The magnetic field was set zero during the measurement of both devices.

pair density.

The cavity resonance is fully suppressed at $B_y = 0.7$ T. Notably, up to the field of 0.3 T, the shape of the resonance dip remains nearly unchanged. Figure 4(b) shows the gate response of the resonance at different fields. V was fixed at -2 mV. At B_y of 0.2 T, the resonance is nearly identical to that in the 0.0 T case. Next, we fixed the frequency at its resonance for each field, and measure the rf response $V_{\rm rf}$ and conductance G simultaneously. Figure 4(c) shows their relation at each field. To better visualize their comparison, we add a vertical offset for each curve so that all curves are aligned at $G = 2.5 \times 2e^2/h$. The mapping barely changes for fields below 0.4 T. This field value exceeds the field range of robust zero modes (near 0.2 T), demonstrating the compatibility of our rf technique with Majorana search and control. For fields above 0.4 T, the range of $V_{\rm rf}$ starts to shrink due to the degradation of the resonator.

For completeness, we have also tested the resonator response for in-plane fields, i.e. B_z and B_x, shown in Appendix Fig. 8. For those directions, the resonator can sustain for B up to 1 T before degradation.

V. RESISTIVE AND CAPACITIVE SENSING OF PbTe NANOWIRES

Besides the NS device, we also implement this rf technique on PbTe field effect devices. Figure 5(a) shows its false-color SEM. The PbTe nanowire is contacted by two metallic leads (yellow), and then covered by a thin layer of Al_2O_3 dielectric and a top gate (green). The rf probe is connected to the source, similar to the NS device. Figure 5(b) shows the reflected amplitude $|S_{21}|$ as a function of the top gate voltage V_G and the rf frequency f. Line cuts at several gate voltages are plotted in Fig. 5(c). Compared to Fig. 2, the resonance here is deeper, reaching 10 dB for $G = 3.14 \times 2e^2/h$ (see the pink curve in Fig. 5(c). The sharper resonance is due to an improved impedance matching. The PCB design is different from that of the NS device. Parameters of the circuit elements are: $C_{\rm fixed}$ = 0.2 pF, $C_{\rm parasitic}$ = 4.3 pF, $L_{\rm spiral}$ = 520 nH, $R_{\rm dissipation}$ = 2.5 kΩ (the rest elements are identical to those in Fig. 1(b)). We calculate the circuit impedance at the resonance frequency (f = 167 MHz) to be 27.9 − 2.7i (Ω) for $G = 3 \times 2e^2/h$. While this impedance is still not matched to 50 Ω, it is much closer than that of the NS device. Since the impedance is smaller than 50 Ω, a decrease in conductance further decreases the impedance. Correspondingly, the dip becomes shallower, exhibiting an opposite trend in the V_G scan compared to that in Fig. 2(a). Figure 5(d) shows the simulated resonator response for different device conductance using the parameters mentioned above. The simulation qualitatively captures the experimental results in Fig. 5(c).

For another field effect device, we connect the rf probe to the top gate instead of the contact, as shown in Fig. 5(e). For the resistive sensing, the resonance frequency

barely changes but the sharpness of the resonance dip varies when tuning the device conductance. Here, V_G tunes the capacitance, causing a shift in the resonance frequency. Figure 5(f) shows the gate scan. The resonance frequency shifts by ~ 1.2 MHz when V_G is scanned from 0.0 V to 2.0 V, see line cuts in Fig. 5(g).

The device capacitance is governed by the gate geometry (area and dielectric thickness) as well as the electron distribution in the PbTe nanowire. The former is fixed once the device is fabricated while the latter can be affected by V_G. A more positive V_G attracts more electrons to the nanowire top surface. This accumulation layer shortens the effective spacing between the capacitor plates and increases the capacitance. The resonance frequency ($f_C = 1/(2\pi\sqrt{LC})$) thus decreases, as shown in Fig. 5(f). The device conductance as a function of V_G is shown in Fig. 5(h). The conductance fluctuations are not correlated with the resonance frequencies during the V_G scan. Moreover, the resonance continues to shift towards higher frequencies even after the device is pinched off. We attribute this to gate-induced charges in the CdTe substrate. The conduction band of CdTe is only 0.3 eV above that of PbTe. It is possible that V_G may deplete electrons from PbTe into CdTe.

VI. CONCLUSION AND OUTLOOK

In conclusion, we have implemented the radio-frequency reflectometry on PbTe and PbTe-Pb nanowire devices. For resistive sensing, the data-acquisition time can be shortened by an order of magnitude compared to traditional dc measurement. The effect of CdTe substrate is quantified by a dissipation resistor. For the capacitive sensing, a gate-tunable cavity shift is observed. We further demonstrate the compatibility of this rf setup with magnetic field, especially in the field range where signatures of Majorana zero modes have been reported. Our results enable radio-frequency experiments on PbTe quantum devices. Future efforts could focus on improved design of the printed circuit board (e.g. by including in-situ tunable capacitors) for better impedance matching and reduction of substrate dissipation.

VII. DATA AVAILABILITY

The data that support the findings of this article will be openly available soon.

VIII. ACKNOWLEDGMENT

This work is supported by National Natural Science Foundation of China (92565302) and Quantum Science and Technology-National Science and Technology Major Project (2021ZD0302400). W. S. acknowledges the Postdoctoral Fellowship Program and China Postdoctoral Science Foundation (Grant No. BX20250167 and No. 2025M783399).

Appendix A: Methods

Spiral inductor fabrication. A 100-nm-thick Nb film was sputtered on a sapphire substrate. The film was then covered by a photo-resist (S1813, 3000 rpm), and baked at 115 °C for 90 s. Patterns including spiral inductors, bias tee, and bonding pads were defined using direct laser writing. The chip was developed in MF319 for 45 s, followed by reactive ion etching (SF_6, 30 sccm Ar, 10 sccm for 100 s). The residual resist was removed in acetone.

Nanowire growth and device fabrication Three PbTe nanowire devices were studied, including one PbTe-Pb NS device and two PbTe field effect devices. The nanowires were grown selectively on a CdTe substrate. The PbTe-Pb nanowire consists of a 8 nm $Pb_{0.99}Eu_{0.01}Te$ buffer layer, 30 nm PbTe, 5 nm $Pb_{0.97}Eu_{0.03}Te$ spacing layer, 7 nm Pb and 11 nm CdTe capping layer. The PbTe nanowire used in resistive sensing consists of 5 nm $Pb_{0.97}Eu_{0.03}Te$ buffer layer, 12.5 nm PbTe, 5 nm $Pb_{0.95}Eu_{0.05}Te$ capping layer. The PbTe nanowire used in capacitive sensing consists of 5 nm $Pb_{0.99}Eu_{0.01}Te$ buffer layer, 12 nm PbTe, 5 nm $Pb_{0.99}Eu_{0.01}Te$ and 11 nm CdTe capping layer. Details of the growth can be found in Ref. [20].

The fabrication of PbTe nanowires consists of three e-beam lithography steps. First, Ti/Au metallic contacts were deposited. Prior to the contact deposition, in situ Ar plasma etching was performed to remove the surface oxides and PbEuTe/CdTe capping layer. Then an Al_2O_3 dielectric layer was deposited using atomic layer deposition. Finally, top gates were deposited by evaporating Ti/Au. For the PbTe-Pb device, prior to these steps, most of the Pb film on the substrate was etched using Ar ion milling to prevent short circuiting.

Fitting. In Fig. 2(d), we assume a polynomial relationship between $\ln G$ and $V_{\rm rf}$:

$$\begin{aligned}\ln G =& a_6 \cdot (V_{\rm rf})^6 + a_5 \cdot (V_{\rm rf})^5 + a_4 \cdot (V_{\rm rf})^4 + a_3 \cdot (V_{\rm rf})^3 \\ &+ a_2 \cdot (V_{\rm rf})^2 + a_1 \cdot (V_{\rm rf}) + a_0,\end{aligned} \tag{A1}$$

as this guarantees $G > 0$. We find that a polynomial expression up to $(V_{\rm rf})^6$ can give precise and satisfactory fit shown as the red curve in Fig. 2(d). Here, $V_{\rm rf}$ is in units of μV, $a_6 = -5.58587503 \times 10^{-11}$, $a_5 = 1.34033713 \times 10^{-7}$, $a_4 = -1.33805403 \times 10^{-4}$, $a_3 = 7.11366689 \times 10^{-2}$, $a_2 = -2.12427991 \times 10^{1}$, $a_1 = 3.37849600 \times 10^{3}$, $a_0 = -2.23587555 \times 10^{5}$.

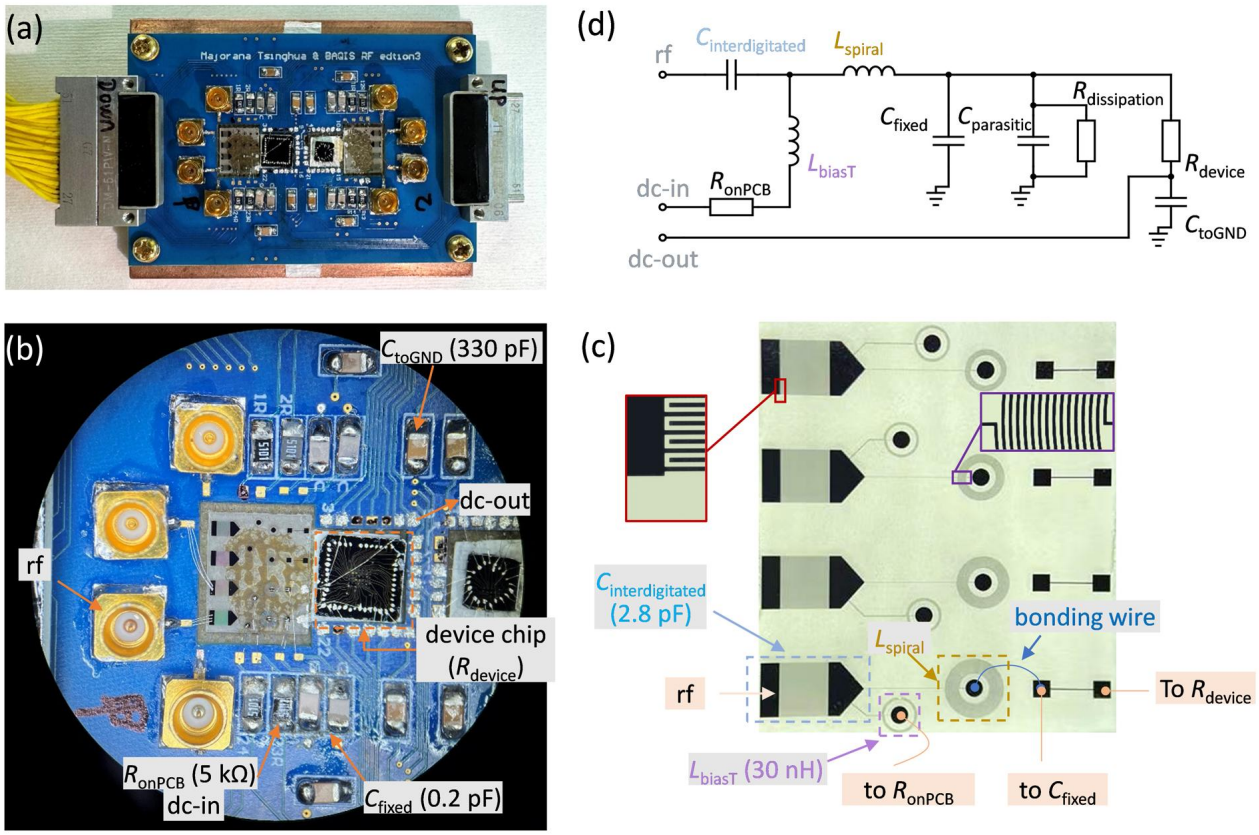

FIG. 6. (a) Optical image (full range) of the PCB. (b) Zoom-in of the left part of the PCB. (c) Optical image of the sapphire substrate before gluing onto the PCB. (d) Circuit diagram, replotted from Fig. 1(b).

Appendix B: Details of the PCB circuit

Figure 6(a) shows a full image of the PCB, mounted (screw tightened) on a copper block. Two device chips were loaded into the voids near the PCB center. Each chip was assigned with 4 rf ports (mini-SMP connectors). The NS device corresponds to the circuit on the left part of the PCB, shown in Fig. 6(b). The device chip is marked by the orange dashed box. The sapphire substrate that carries the interdigitated capacitors and spiral inductors is glued on the left side of the device chip. Figure 6(c) shows this substrate before mounting onto the PCB. The black regions are sputtered Nb superconducting film (100 nm thick), while the rest regions are the sapphire substrate. For comparison, we replot the circuit diagram in Fig. 6(d) and labeled the corresponding elements in Figs. 6(b-c). Insets in (c) are zoom-in images of the capacitor and the inductor.

Appendix C: Circuit simulation

Figure 7 shows the simulated $|S_{21}|$ for the circuits of NS device by varying the device conductance between 0 and $2e^2/h$. We find that by setting $R_{\rm dissipation}$ to be 4 kΩ, the variation of the resonance dip ($\sim$ 2 dB) can be aligned with our result in Fig. 2(b). The parameters of other circuit elements are labeled in Fig. 1(b).

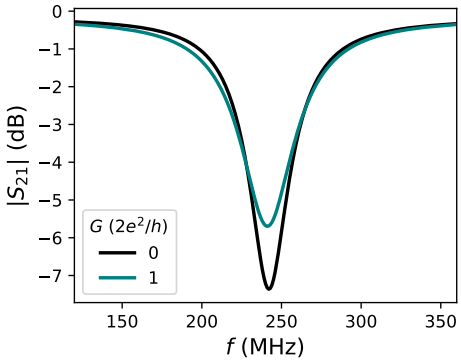

FIG. 7. $|S_{21}|$ simulation for $G = 0$ (black) and $2e^2/h$ (green). $R_{\rm dissipation} = 4$ kΩ.

Appendix D: rf response to in-plane magnetic field

Figure 8 shows the cavity response for magnetic fields applied parallel to the device chip and the sapphire sub-

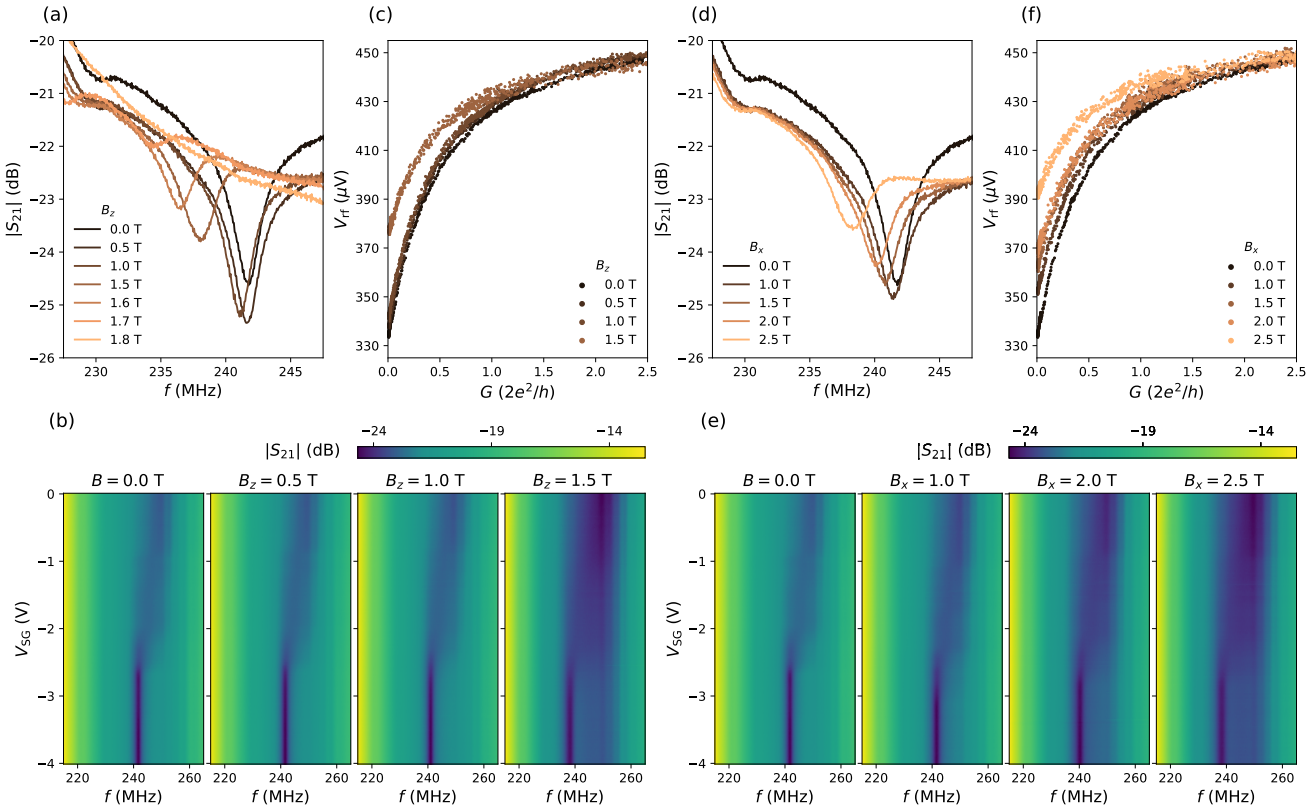

FIG. 8. (a-c) and (d-f) are similar to that in Fig. 4, but for B_z and B_x, respectively. $V_{TG} = -5$ V, $V = -2$ mV. $V_{SG} = -4$ V for (a) and (d). For (c) and (f), vertical offset was added to each curve so that V_{rf} values at $G = 2.5e^2/h$ are all aligned.

strate. The spiral inductor can remain superconducting for larger in-plane fields due to less orbital effect. Correspondingly, the resonance dip size barely changes up to 1 T for both B_z and B_x, as shown in Figs. 8(a) and 8(d). This is also evident by the V_{rf} vs G mapping in Figs. 8(c) and 8(d). The resonance frequency decreases for increasing B.

[1] Z. Cao, D. E. Liu, W.-X. He, X. Liu, K. He, and H. Zhang, Numerical study of PbTe-Pb hybrid nanowires for engineering Majorana zero modes, Phys. Rev. B **105**, 085424 (2022).

[2] Y. Jiang, S. Yang, L. Li, W. Song, W. Miao, B. Tong, Z. Geng, Y. Gao, R. Li, F. Chen, Q. Zhang, F. Meng, L. Gu, K. Zhu, Y. Zang, R. Shang, Z. Cao, X. Feng, Q.-K. Xue, D. E. Liu, H. Zhang, and K. He, Selective area epitaxy of PbTe-Pb hybrid nanowires on a lattice-matched substrate, Phys. Rev. Materials **6**, 034205 (2022).

[3] J. Jung, S. G. Schellingerhout, M. F. Ritter, S. C. ten Kate, O. A. van der Molen, S. de Loijer, M. A. Verheijen, H. Riel, F. Nichele, and E. P. Bakkers, Selective area growth of PbTe nanowire networks on InP, Advanced Functional Materials **32**, 2208974 (2022).

[4] R. M. Lutchyn, J. D. Sau, and S. Das Sarma, Majorana fermions and a topological phase transition in semiconductor-superconductor heterostructures, Phys. Rev. Lett. **105**, 077001 (2010).

[5] Y. Oreg, G. Refael, and F. von Oppen, Helical liquids and Majorana bound states in quantum wires, Phys. Rev. Lett. **105**, 177002 (2010).

[6] C. Nayak, S. H. Simon, A. Stern, M. Freedman, and S. Das Sarma, Non-Abelian anyons and topological quantum computation, Rev. Mod. Phys. **80**, 1083 (2008).

[7] Z. Geng, Z. Zhang, F. Chen, S. Yang, Y. Jiang, Y. Gao, B. Tong, W. Song, W. Miao, R. Li, Y. Wang, Q. Zhang, F. Meng, L. Gu, K. Zhu, Y. Zang, L. Li, R. Shang, X. Feng, Q.-K. Xue, K. He, and H. Zhang, Observation of Aharonov-Bohm effect in PbTe nanowire networks, Phys. Rev. B **105**, L241112 (2022).

[8] S. C. ten Kate, M. F. Ritter, A. Fuhrer, J. Jung, S. G. Schellingerhout, E. P. A. M. Bakkers, H. Riel, and F. Nichele, Small charging energies and g-factor anisotropy in PbTe quantum dots, Nano Letters **22**, 7049 (2022).

[9] Z. Zhang, W. Song, Y. Gao, Y. Wang, Z. Yu, S. Yang, Y. Jiang, W. Miao, R. Li, F. Chen, Z. Geng, Q. Zhang, F. Meng, T. Lin, L. Gu, K. Zhu, Y. Zang, L. Li, R. Shang, X. Feng, Q.-K. Xue, K. He, and H. Zhang, Proximity effect in PbTe-Pb hybrid nanowire Josephson junctions, Phys. Rev. Mater. **7**, 086201 (2023).

[10] W. Song, Y. Wang, W. Miao, Z. Yu, Y. Gao, R. Li, S. Yang, F. Chen, Z. Geng, Z. Zhang, S. Zhang, Y. Zang, Z. Cao, D. E. Liu, R. Shang, X. Feng, L. Li, Q.-K. Xue, K. He, and H. Zhang, Conductance quantization in PbTe nanowires, Phys. Rev. B **108**, 045426 (2023).

[11] Y. Gao, W. Song, S. Yang, Z. Yu, R. Li, W. Miao, Y. Wang, F. Chen, Z. Geng, L. Yang, Z. Xia, X. Feng, Y. Zang, L. Li, R. Shang, Q.-K. Xue, K. He, and H. Zhang, Hard superconducting gap in PbTe nanowires, Chinese Physics Letters **41**, 038502 (2024).

[12] Y. Wang, F. Chen, W. Song, Z. Geng, Z. Yu, L. Yang, Y. Gao, R. Li, S. Yang, W. Miao, W. Xu, Z. Wang, Z. Xia, H.-D. Song, X. Feng, T. Wang, Y. Zang, L. Li, R. Shang, Q. Xue, K. He, and H. Zhang, Ballistic PbTe nanowire devices, Nano Letters **23**, 11137 (2023).

[13] R. Li, W. Song, W. Miao, Z. Yu, Z. Wang, S. Yang, Y. Gao, Y. Wang, F. Chen, Z. Geng, L. Yang, J. Xu, X. Feng, T. Wang, Y. Zang, L. Li, R. Shang, Q. Xue, K. He, and H. Zhang, Selective-area-grown PbTe-Pb planar Josephson junctions for quantum devices, Nano Letters **24**, 4658 (2024).

[14] M. Gupta, V. Khade, C. Riggert, L. Shani, G. Menning, P. J. H. Lueb, J. Jung, R. Mélin, E. P. A. M. Bakkers, and V. S. Pribiag, Evidence for π-shifted cooper quartets and few-mode transport in pbte nanowire three-terminal josephson junctions, Nano Letters **24**, 13903 (2024).

[15] Z. Geng, F. Chen, Y. Gao, L. Yang, Y. Wang, S. Yang, S. Zhang, Z. Li, W. Song, J. Xu, *et al.*, Enhanced superconductivity in PbTe-In hybrids, Phys. Rev. Mater. **9**, 084802 (2025).

[16] Y. Gao, W. Song, Z. Yu, S. Yang, Y. Wang, R. Li, F. Chen, Z. Geng, L. Yang, J. Xu, Z. Wang, Z. Li, S. Zhang, X. Feng, T. Wang, Y. Zang, L. Li, R. Shang, Q.-K. Xue, K. He, and H. Zhang, SQUID oscillations in PbTe nanowire networks, Phys. Rev. B **110**, 045405 (2024).

[17] Z. Li, W. Song, S. Zhang, Y. Wang, Z. Wang, Z. Yu, R. Li, Z. Yan, J. Xu, Y. Gao, S. Yang, L. Yang, X. Feng, T. Wang, Y. Zang, L. Li, R. Shang, Q.-K. Xue, K. He, and H. Zhang, Anisotropy of PbTe nanowires with and without a superconductor, Phys. Rev. B **111**, 195416 (2025).

[18] Y. Wang *et al.*, Presence versus absence of charging energies in PbTe quantum dots, arXiv: 2602.12791 (2026).

[19] Y. Wang, W. Song, Z. Cao, Z. Yu, S. Yang, Z. Li, Y. Gao, R. Li, F. Chen, Z. Geng, L. Yang, J. Xu, Z. Wang, S. Zhang, X. Feng, T. Wang, Y. Zang, L. Li, R. Shang, Q.-K. Xue, D. E. Liu, K. He, and H. Zhang, Gate-tunable subband degeneracy in semiconductor nanowires, Proceedings of the National Academy of Sciences **121**, e2406884121 (2024).

[20] W. Song, Z. Yu, Y. Wang, Y. Gao, Z. Li, S. Yang, S. Zhang, Z. Geng, R. Li, Z. Wang, *et al.*, Reducing disorder in PbTe nanowires for Majorana research, Nano Letters **25**, 2350 (2025).

[21] Y. Gao, W. Song, Y. Wang, Z. Geng, Z. Cao, Z. Yu, S. Yang, J. Xu, F. Chen, Z. Li, *et al.*, Quantized Andreev conductance in semiconductor nanowires, Phys. Rev. Appl. **23**, L061004 (2025).

[22] S. Zhang, W. Song, Z. Li, Z. Yu, R. Li, Y. Wang, Z. Yan, J. Xu, Z. Wang, Y. Gao, S. Yang, L. Yang, X. Feng, T. Wang, Y. Zang, L. Li, R. Shang, Q.-K. Xue, K. He, and H. Zhang, Strong enhancement of g-factor in PbTe–Pb hybrid nanowires, Nano Letters **26**, 4739 (2026).

[23] R. Li *et al.*, Gate-tunable superconductor-semiconductor coupling and its impact on zero-energy modes in PbTe-Pb nanowires, (to be appeared) (2026).

[24] S. Plugge, A. Rasmussen, R. Egger, and K. Flensberg, Majorana box qubits, New Journal of Physics **19**, 012001 (2017).

[25] T. Karzig, C. Knapp, R. M. Lutchyn, P. Bonderson, M. B. Hastings, C. Nayak, J. Alicea, K. Flensberg, S. Plugge, Y. Oreg, C. M. Marcus, and M. H. Freedman, Scalable designs for quasiparticle-poisoning-protected topological quantum computation with Majorana zero modes, Phys. Rev. B **95**, 235305 (2017).

[26] D. J. Reilly, C. M. Marcus, M. P. Hanson, and A. C. Gossard, Fast single-charge sensing with a rf quantum point contact, Applied Physics Letters **91**, 162101 (2007).

[27] M. D. Schroer, M. Jung, K. D. Petersson, and J. R. Petta, Radio frequency charge parity meter, Phys. Rev. Lett. **109**, 166804 (2012).

[28] N. Ares, F. J. Schupp, A. Mavalankar, G. Rogers, J. Griffiths, G. A. C. Jones, I. Farrer, D. A. Ritchie, C. G. Smith, A. Cottet, G. A. D. Briggs, and E. A. Laird, Sensitive radio-frequency measurements of a quantum dot by tuning to perfect impedance matching, Phys. Rev. Appl. **5**, 034011 (2016).

[29] D. Razmadze, D. Sabonis, F. K. Malinowski, G. C. Ménard, S. Pauka, H. Nguyen, D. M. van Zanten, E. C. O'Farrell, J. Suter, P. Krogstrup, F. Kuemmeth, and C. M. Marcus, Radio-Frequency methods for Majorana-based quantum devices: Fast charge sensing and phase-diagram mapping, Phys. Rev. Appl. **11**, 064011 (2019).

[30] D. M. T. van Zanten, D. Sabonis, J. Suter, J. I. Väyrynen, T. Karzig, D. I. Pikulin, E. C. T. O'Farrell, D. Razmadze, K. D. Petersson, P. Krogstrup, and C. M. Marcus, Photon-assisted tunnelling of zero modes in a Majorana wire, Nature Physics **16**, 663 (2020).

[31] F. K. Malinowski, L. Han, D. de Jong, J.-Y. Wang, C. G. Prosko, G. Badawy, S. Gazibegovic, Y. Liu, P. Krogstrup, E. P. Bakkers, L. P. Kouwenhoven, and J. V. Koski, Radio-Frequency C-V measurements with subattofarad sensitivity, Phys. Rev. Appl. **18**, 024032 (2022).

[32] F. Vigneau, F. Fedele, A. Chatterjee, D. Reilly, F. Kuemmeth, M. F. Gonzalez-Zalba, E. Laird, and N. Ares, Probing quantum devices with radio-frequency reflectometry, Applied Physics Reviews **10**, 021305 (2023).